ACS APPLIED MATERIALS & INTERFACES

www.acsami.org
Research Article

A Mg^{2+}-Regulated Hydrated Vanadium Oxide Positive Electrode for Aqueous Mg-Ion Batteries

Qiang Fu,* Xianlin Luo, Liwen Yang, Angelina Sarapulova, Michael Knapp, Helmut Ehrenberg, and Sonia Dsoke

Cite This: https://doi.org/10.1021/acsami.5c08636 Read Online

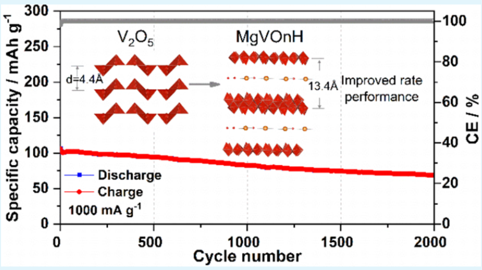

ABSTRACT: Aqueous Mg-ion batteries (AMIBs) have emerged as promising candidates for grid-level energy storage systems, thanks to their exceptional safety characteristics, cost-effectiveness, and abundant Mg resources. However, AMIBs confront great challenges, such as the shortage of high-performance electrodes and the sluggish Mg^{2+} diffusion in the electrodes. In this work, a Mg^{2+}-regulated bilayered vanadium oxide (MgVOnH) positive electrode, holding a large interplanar spacing of ~13.4 Å, was investigated in 0.8 m $Mg(TFSI)_2$−85% poly(ethylene glycol) (PEG)−15% H_2O and 0.8 m $Mg(TFSI)_2$−65% PEG−20% dimethyl sulfoxide (DMSO)−15% H_2O (20% DMSO-containing) electrolytes. MgVOnH delivers a first discharge capacity of 268 mAh g^{-1} at 50 mA g^{-1}, obtaining 81% capacity retention after 100 cycles (against a second discharge capacity of 249 mAh g^{-1}) in a DMSO-free electrolyte, whereas MgVOnH exhibits much better rate capability and high capacity at 500 and 1000 mA g^{-1} in the DMSO-containing electrolyte, respectively. Particularly, MgVOnH shows a first discharge capacity of 106 mAh g^{-1} at 1000 mA g^{-1}, maintaining 80/65% of its capacity after 920/2000 cycles. Furthermore, the electrochemical reaction mechanism and reversibility of MgVOnH during Mg^{2+} (de)intercalation are systematically explored through ex situ techniques. This work helps us to understand the mechanisms, and this can guide us in achieving a better design for high-performance positive electrodes for AMIBs.

KEYWORDS: *aqueous Mg-ion batteries, vanadium oxide positive electrode, large interlayer spacing, high capacity, electrochemical performance*

1. INTRODUCTION

Aqueous magnesium-ion batteries (AMIBs) are regarded as attractive contenders for application in large-scale energy storage owing to their economic viability, intrinsic safety, and rich Mg resources.[1−5] Compared with non-aqueous electrolytes (about 10 mS cm^{-1}), aqueous electrolytes exhibit superior ionic transport characteristics, such as higher ionic conductivity (up to 1000 mS cm^{-1}), leading to higher rate capability and lower activation energy of charge transfer.[6−8] Moreover, the manufacturing cost of AMIBs is lower than that of organic-based systems thanks to the non-toxic and inflammable properties of aqueous electrolytes and non-strict humidity control during cell preparation.[9,10]

Recently, researchers have made significant progress in the development of AMIBs components, including aqueous Mg-ion electrolytes (AMEs) and positive/negative electrodes. For instance, Xia et al.[11] designed a full AMIB, including a Prussian blue positive electrode, a polyimide negative electrode, and 1 M $MgSO_4$ electrolyte, which demonstrates a plateau at 1.3 V and a low discharge capacity of 35 mAh g^{-1} (energy density of 45 Wh kg^{-1}). Note that an aqueous electrolyte often suffers from the risk of hydrogen evolution when exceeding 1.23 V, which can be limited due to the use of concentrated electrolytes. Wang et al.[2] applied $Mg_xLiV_2(PO_4)_3$ and poly pyromellitic dianhydride (PPMDA) in 4 m ("m" means "mol kg^{-1}") magnesium bis(trifluoromethanesulfonyl)imide ($Mg(TFSI)_2$), where the AME had an expanded electrochemical stability window (ESW) of 2.0 V and therefore enhanced the energy density of AMIBs to 62.4 Wh kg^{-1}. Alshareef et al. reported an aqueous Mg^{2+}-based dual-ion full-cell,[12] which consists of a polyaniline (PANI) positive electrode, a polyimide negative electrode, and saturated 4.5 m $Mg(NO_3)_2$ electrolyte, and a full AMIB based on Prussian blue and an organic negative electrode by designing a hydrated eutectic electrolyte $Mg(NO_3)_2{\cdot}6H_2O$−acetamide[13] with an extended ESW of 2.7 V. Both of them display excellent stability and rate performance, but low capacity. Recently, the ESW of AME was expanded up to 3.7 V by tuning their physical−chemical properties using polyethylene glycol (PEG),[14] and then the transport properties of AME (increased ionic conductivity and lowered viscosity) were further improved by adding dimethyl

Received: April 30, 2025
Revised: November 2, 2025
Accepted: November 25, 2025

sulfoxide (DMSO) without sacrificing its ESW (~3.6 V), which enabled a much-improved rate capability and capacity of vanadium oxides.[15] Apart from that, Mn-based oxide positive electrodes, such as MnO_2,[16−18] Mn_3O_4,[19] $MgMn_2O_4$,[20,21] $Mg_{1.1}Mn_6O_{12}\cdot 4.5H_2O$,[22] and $MgFe_xMn_{2-x}O_4$,[23] were also reported. However, AMIBs still face great challenges, such as the shortage of high-performance electrodes, which often suffer from sluggish Mg^{2+} migration kinetics in the electrodes. Note that Mg metal cannot be used as a negative electrode due to its incompatibility in the aqueous system. Consequently, developing high-performance electrode materials is a critical necessity for safe, high-energy, and sustainable AMIBs.

Vanadium pentoxide (V_2O_5) receives much attention as a positive electrode thanks to its two-dimensional lattice architecture and large specific capacity (294 mAh g^{-1}, 1 mol of Mg^{2+} per mol V_2O_5). For example, metastable ζ-V_2O_5 was reported in a non-aqueous Mg-ion system to provide a discharge capacity of 140 mAh g^{-1} for the first cycle and of 90 mAh g^{-1} over 50 cycles at 50 °C.[24] Yoo et al.[25] addressed that α-V_2O_5 showed a specific capacity of 295 mAh g^{-1} with high reversibility at a low current density of C/20 under 110 °C in an ionic liquid electrolyte. Moreover, α-V_2O_5 was reported to deliver a high initial discharge capacity of 359 mAh g^{-1} and 80% of its capacity over 100 cycles in PEG-containing AME.[14] However, V_2O_5 suffers from sluggish Mg^{2+} diffusion and shows a limited rate capability. In contrast, bilayered vanadium oxide ($V_2O_5\cdot nH_2O$) exhibits a large d-spacing of ~11.5 Å and facilitates ionic diffusion due to the charge shielding of Mg^{2+} by crystal water.[21] Besides, Mg^{2+}- and Mn^{4+}-preintercalated bilayered vanadium oxides are supposed to hold higher structural stability during Mg^{2+} (de)intercalation in non-aqueous Mg-ion systems because of the formed "pillars" with O atoms.[26,27] For instance, $Mg_{0.3}V_2O_5\cdot 1.1H_2O$ showed a first specific capacity of 164 mAh g^{-1} at 100 mA g^{-1} without capacity decay over 500 cycles in a non-aqueous Mg-ion system.[27] $Mn_{0.04}V_2O_5\cdot 1.17H_2O$ exhibited a capacity of 145 mAh g^{-1} for the first discharge at 50 mA g^{-1} without capacity decay over 100 cycles and a maximum capacity of 97 mAh g^{-1} at 1000 mA g^{-1} with a capacity retention of 90% over 5000 cycles.[21] We reported Ca^{2+}-preintercalated bilayered vanadium oxide (CaVOnH), delivering a specific capacity of 273 mAh g^{-1} at a current density of 50 mA g^{-1} in PEG-containing AME, and found that it needs over 100 cycles to reach their highest capacities for both CaVOnH and V_2O_5 in the DMSO-containing electrolyte.[15] The effect of interplanar spacing (crystal water) of vanadium oxide on electrochemical performance remains unclear.

Herein, to bridge a critical knowledge gap in structure−performance relationships, we designed a novel Mg^{2+}-regulated hydrated vanadium oxide (MgVOnH) featuring an exceptionally large interplanar spacing of ~13.4 Å—the highest reported for bilayered vanadium oxides in aqueous Mg-ion batteries (AMIBs). Moreover, MgVOnH is prepared via a hydrothermal method that leverages the strong structural affinity of Mg^{2+} (ionic radius: 0.72 Å) to expand the interlayer beyond CaVOnH (~13 Å, Ca^{2+} radius: 1.00 Å).[28] Crucially, we establish a direct correlation between interlayer hydration and electrochemical performance by systematically comparing MgVOnH with CaVOnH and V_2O_5 in both DMSO-free and DMSO-containing electrolytes operating between 1.58 and 3.68 V vs Mg^{2+}/Mg, where the latter one grants a significantly enhanced rate capability and higher capacity. In addition, the underlying electrochemical mechanism of MgVOnH is analyzed using a combination of ex situ techniques, namely, X-ray powder diffraction (XRD), Raman scattering, X-ray absorption spectroscopy (XAS), and X-ray photoelectron spectroscopy (XPS). This work presents an in-depth understanding that would help design high-safety, low-cost, and high-performance positive electrodes for AMIBs.

2. EXPERIMENTAL SECTION

2.1. Synthesis of $Mg_xV_2O_5\cdot nH_2O$ Nanowires (MgVOnH)

MgVOnH nanowires were prepared via a hydrothermal route, which is similar to our previous report.[15] The synthesis began by vigorously stirring 0.5 g of commercial V_2O_5 powder (Alfa Aesar, 99.99%) into 20 mL of deionized water for 10 min, yielding a light orange suspension. Subsequently, 5 mL of 30% hydrogen peroxide (H_2O_2) was introduced dropwise to this suspension under continuous stirring. After 20 min of reaction, a clear and reddish-brown solution was obtained. Following this, an aqueous solution of 0.1474 g of $Mg(CH_3COO)_2\cdot 4H_2O$ in 5 mL of deionized water was prepared and added to the reddish-brown solution, with stirring continued for an additional 10 min. The final mixture was sealed in a 50 mL Teflon-lined stainless steel autoclave and subjected to a thermal treatment at 200 °C for 48 h. The resulting solid product was collected, thoroughly washed with deionized H_2O and ethanol, and finally dried at 75 °C for 12 h. Warning Note: there is a safety risk in the case of too high pressure in the autoclave in the case of using too much solutions, and amounts and temperature need to be carefully adjusted to the vessel.

2.2. Preparation of Electrolytes

0.8 m $Mg(TFSI)_2$−(85% − x)PEG−xDMSO−15% H_2O (x = 0 and 20%) electrolyte was prepared by dissolving the salt in a hybrid solvent system composed of polyethylene glycol 400 (PEG 400), dimethyl sulfoxide (DMSO), and pure H_2O solvent under vigorous stirring at room temperature for 12 h.

2.3. Morphological and Structural Study

To investigate the material's properties, a comprehensive morphological and structural analysis was conducted. Scanning electron microscopy (SEM) imaging and energy-dispersive X-ray spectroscopy (EDS) were performed by using a Zeiss Supra 55 microscope operating at a 15 keV primary energy. For structural analysis, powder X-ray diffraction (XRD) patterns were acquired on a STOE STADI P diffractometer using Mo Kα_1 radiation (λ = 0.70932 Å). Samples were prepared by loading the powder into 0.5 mm Ø borosilicate capillaries, and data were collected in a capillary geometry. The water content within the crystal structure was determined by thermogravimetric analysis (TGA) using a Netzsch STA 449C instrument under a flowing argon atmosphere. Furthermore, Raman spectra were recorded on a Horiba Scientific LabRam HR Evolution microscope configured with a 633 nm HeNe laser (17 mW power), a 600 gr mm^{-1} grating, and a charge-coupled device (CCD) detector. A 100× objective lens (numerical aperture (NA) 0.95) was used for all measurements on both pristine and cycled electrodes.

X-ray photoelectron spectroscopy (XPS) measurements were performed using a K-Alpha spectrometer (Thermo Fisher Scientific, U.K.). This instrument features a microfocused, monochromated Al Kα X-ray source (λ = 1486.6 eV) and was operated with a 400 μm spot size. To mitigate surface charging, a charge compensation system employing 8 eV electrons and low-energy argon ions was utilized. All specimens were prepared within an argon-filled glovebox and introduced into the analysis chamber via an inert transfer protocol to prevent air exposure. Data were collected and processed using Thermo Avantage software, as described elsewhere.[29] Quantitative analysis incorporated the analyzer transmission function, Scofield sensitivity factors, and effective attenuation lengths of photoelectrons,[30] with the latter being determined using the standard TPP-2 M formalism.[31] All binding energies were calibrated by setting the carbonaceous C 1s peak (C−C/C−H) to 285.0 eV.

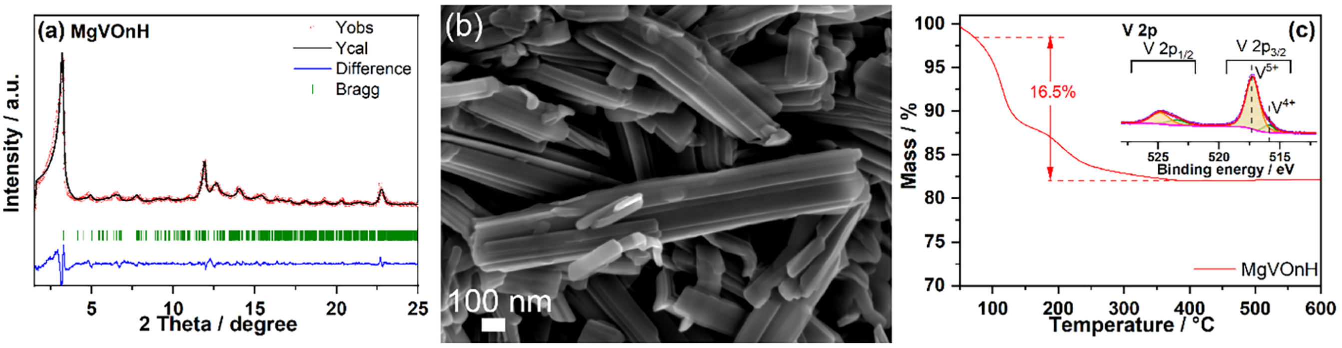

Figure 1. Le Bail fitting based on X-ray diffraction data (a) (Mo $K_{\alpha 1}$, $\lambda = 0.70932$ Å), SEM image (b), and TGA curve (c) under an Ar atmosphere of pristine MgVOnH (inset: V 2p XPS).

2.4. Electrochemical Characterizations

A slurry was formulated by combining the active material (MgVOnH), conductive carbon (C65, Timcal), and poly(vinylidene difluoride) (PVDF) binder in a mass ratio of 70:20:10, using *N*-methyl-2-pyrrolidone (NMP) as the solvent. This mixture was coated onto stainless steel foil and dried overnight at 65 °C, yielding electrodes with a mass loading of approximately 1.3 mg cm^{-2}. The dried electrodes were punched into 12 mm diameter discs. The activated carbon (AC) counter electrodes were prepared by mixing AC, C65 carbon (Timcal), and a polytetrafluoroethylene (PTFE) binder (60 wt % solution in water, Sigma-Aldrich) in an 8:1:1 mass ratio with isopropanol. The mixture was homogenized using a SpeedMixer (DAC150.1 FVZ model) at 800 rpm for 10 min, manually kneaded on a glass plate, and rolled into a film of uniform thickness. All electrodes were vacuum-dried at 70 °C overnight prior to cell assembly.

Swagelok-type three-electrode cells were assembled under ambient conditions. The cell configuration consisted of a MgVOnH working electrode, an AC counter electrode, a AgCl/Ag reference electrode (3 M NaCl), and 700 μL of $Mg(TFSI)_2$−(85% − x)PEG−xDMSO−15% H_2O ($x = 0$ and 20%) electrolyte (700 μL) as well as a piece of glass microfiber (Whatman) separator. Owing to its high surface area and electrical double-layer capacitance, activated carbon (AC) was employed as the counter electrode to ensure a full charge balance during magnesium intercalation.[24,27] The AC counter electrode was intentionally designed with a large excess mass (N/P ratio ≈ 9−12) to ensure sufficient charge balance during magnesium intercalation. Note that the specific capacity values were calculated based on the mass of the MgVOnH active material. Electrochemical tests, including galvanostatic cycling with potential limitation (GCPL) and cyclic voltammetry (CV), were conducted on a VMP3 potentiostat (BioLogic) at 25 °C. The operating potential window was set between −1.0 and 1.1 V (vs AgCl/Ag, 3 M NaCl). All reported potentials were converted to the Mg^{2+}/Mg scale by subtracting 2.58 V, the known difference between the AgCl/Ag and Mg^{2+}/Mg reference electrodes. Rate capability was assessed by performing GCPL tests at current densities ranging from 50 mA to 1000 mA g^{-1}.

2.5. Sample Preparation for Ex Situ Characterizations

For ex situ characterization, cells containing MgVOnH electrodes were disassembled at specific states of charge and then thoroughly washed with acetonitrile in an argon-filled glovebox. Ex situ X-ray absorption spectroscopy (XAS) measurements were performed at the PETRA-III beamline P65 at DESY in Hamburg. Measurements were conducted at the vanadium K-edge in quick-XAS mode (6 min per spectrum) for MgVOnH at different states, using fluorescence detection with a Passivated Implanted Planar Silicon (PIPS) detector. The energy scale was calibrated using a vanadium metal reference foil. Standard reference compounds (V_2O_5, VO_2, and V_2O_3) were also measured for comparison. All data were acquired at room temperature using a Si(111) double-crystal monochromator and processed with the DEMETER software package.[32]

3. RESULTS AND DISCUSSION

3.1. Structure, Morphology, and Chemical Composition of MgVOnH

X-ray powder diffraction (XRD) was conducted to characterize the structure and phase purity of MgVOnH prepared via the hydrothermal method. The XRD pattern of MgVOnH cannot be indexed with known crystal structures reported in literature, including monoclinic σ-$Mg_{0.25}V_2O_5{\cdot}H_2O$ and δ-$Ca_{0.25}V_2O_5{\cdot}H_2O$, which is composed of V_2O_5 layers stacking along the *c* axis and with cations and water molecules in between interlayers.[33,34] The XRD pattern of MgVOnH is similar to those of e-V_2O_5[35] and e-$M_xV_2O_{5+y}{\cdot}nH_2O$,[36] implying its xerogel structure. Its structure is composed of double-layered $[VO_6]$ octahedra and $[VO_5]$ pyramids, while metal cations and crystal water are located between the interlayers. MgVOnH displays a sharp 001 reflection at $2\theta = \sim 3.2°$, demonstrating the successful preparation of layered vanadium oxide with a larger interlayer distance of ∼13.4 Å, much bigger than those of ζ-V_2O_5 (∼9.5 Å),[24] $NH_4V_4O_{10}$ (9.8 Å),[37] $Zn_{0.25}V_2O_5{\cdot}nH_2O$ (∼10.2 Å),[38] $Mg_{0.3}V_2O_5{\cdot}1.1H_2O$ (∼11.9 Å),[27] and $Ca_{0.219}V_2O_{5+\delta}{\cdot}1.51H_2O$ (CaVOnH, ∼13.0 Å).[15] The large interplanar spacing of MgVOnH supplies more interspace for Mg^{2+} storage and would facilitate Mg^{2+} diffusion. Le Bail fitting demonstrates a compatibility of observed reflections with a triclinic unit cell (Figure 1a) with lattice parameters of a = 10.7798 Å, b = 7.9175 Å, c = 13.3320 Å, α = 90.084°, β = 89.780°, and γ = 89.810°, in agreement with the lattice parameters of $Mg_{0.34}V_2O_5{\cdot}0.84H_2O$.[9] Scanning electron microscopy (SEM) identifies the nanowire morphology of MgVOnH with a typical length between 300 and 3 μm and a width of ∼100 nm (Figure 1b). Energy-dispersive spectroscopy (EDS) demonstrates the homogeneous distribution of Mg, V, and O elements (Figure S1). To estimate the chemical composition in the material, thermogravimetric analysis (TGA), inductively coupled plasma optical emission spectroscopy (ICP-OES), and X-ray photoelectron spectroscopy (XPS) were conducted. MgVOnH demonstrates a total weight loss of ∼16.5% in the range of 100−400 °C, ascribed to crystal water in TGA (Figure 1c) and a ratio of Mg/V of 0.214:2 via ICP-OES. The V 2p XPS profile of MgVOnH exhibits two distinct spin−orbit doublets at 517.2 and 515.9 eV for V $2p_{3/2}$,[39] giving an average vanadium oxidation state of $V^{4.89+}$ (inset of Figure 1c). To reconcile the charge balance, oxygen non-stoichiometry is necessarily introduced in the material, leading to the chemical formula of $Mg_{0.214}V_2O_{5+\delta}{\cdot}nH_2O$ ($\delta \sim 0.11$, $n \sim 2.05$). Overall, it can be clearly seen that MgVOnH has a larger interplanar spacing and more crystal water than

https://doi.org/10.1021/acsami.5c08636

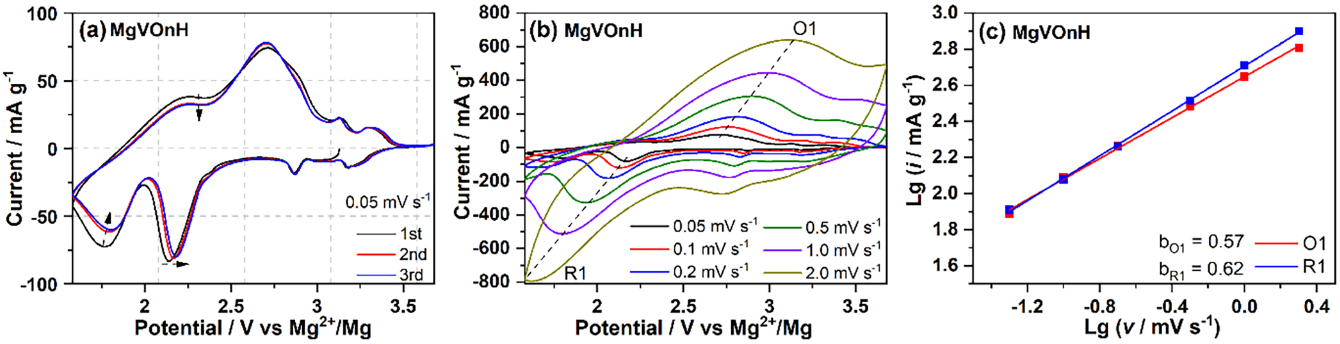

Figure 2. Cyclic voltammetry (CV) profiles acquired at 0.05 mV s^{-1} (a), CV curves measured at various scan rates (b), and corresponding logarithmic plots of current (lg(i)) vs scan rate (lg(ν)) with linear fitting results of MgVOnH (c). The arrows in (a) show the evolution of the redox peaks from the first to the third cycle. All measurements were carried out in a three-electrode configuration, with MgVOnH as the working electrode, activated carbon as the counter electrode, and the AgCl/Ag reference electrode within a voltage window of −1.0 and 1.1 V vs AgCl/Ag. Reported potentials are referenced to the Mg^{2+}/Mg scale for the sake of clarity.

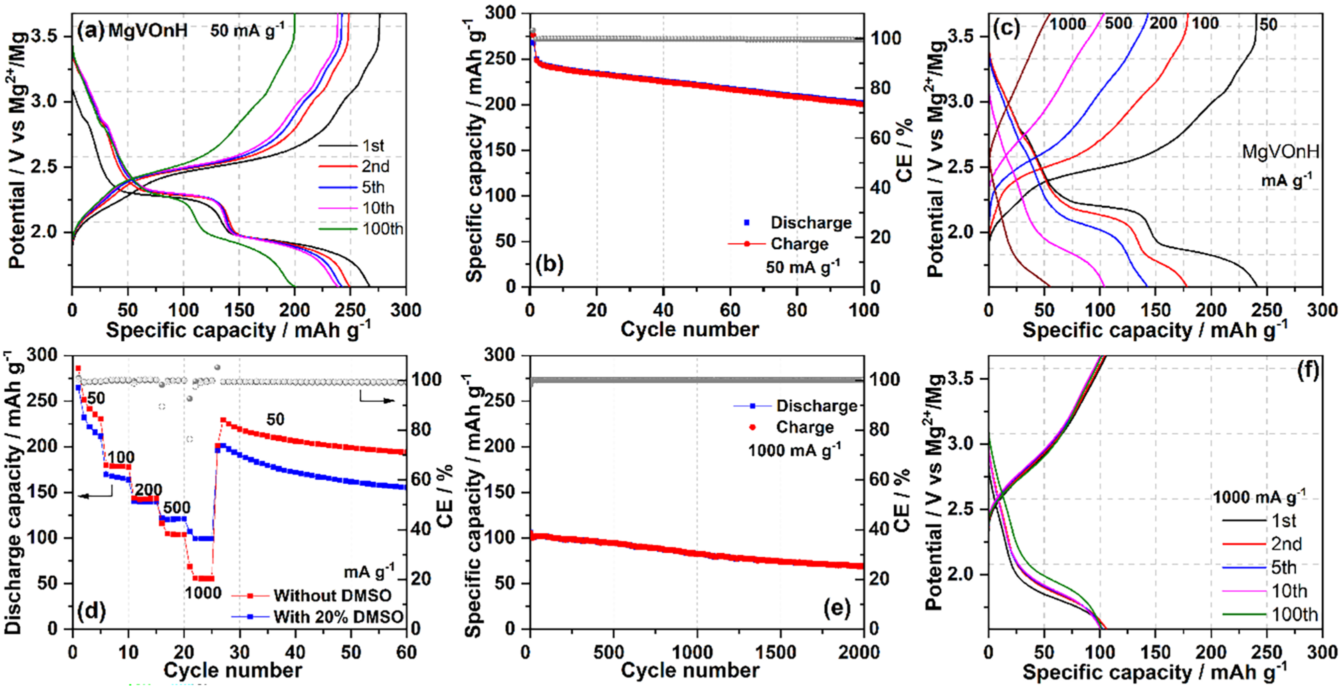

Figure 3. Charge−discharge curves (a), cycling performance measured at 50 mA g^{-1} (b), charge−discharge profiles from rate performance (c), and rate performance (d) of MgVOnH in 0.8 m Mg(TFSI)$_2$−85% PEG−15% H_2O and 0.8 m Mg(TFSI)$_2$−65% PEG−20% DMSO−15% H_2O. Cycling performance (e) and charge−discharge curves (f) of MgVOnH at 1000 mA g^{-1} in 0.8 m Mg(TFSI)$_2$−65% PEG−20% DMSO−15% H_2O.

that of CaVOnH and V_2O_5. Note that since both MgVOnH and CaVOnH have similar amounts of preintercalated ions, the larger interplanar spacing of MgVOnH is caused by the more crystal water because of the stronger interaction between Mg^{2+} ions and layers of MgVOnH.

3.2. Electrochemical Performance of the MgVOnH Positive Electrode

Cyclic voltammetry (CV) was performed for the first three scans at 0.05 mV s^{-1} in the 0.8 m Mg(TFSI)$_2$−85% PEG−15% H_2O electrolyte in a three-electrode configuration (Figure 2a) with an activated carbon counter electrode and a AgCl/Ag reference electrode within a voltage window of −1.0 and 1.1 V vs AgCl/Ag, which have been converted to Mg^{2+}/Mg reference for convenience between 1.58 and 3.68 V vs Mg^{2+}/Mg. The reason why the electrolyte is chosen is due to its wide ESW of ∼3.7 V based on our previous work.[14] For the first scan, MgVOnH displays four pairs of broad reduction/oxidation peaks at around 3.18/3.31, 2.86/3.14, 2.14/2.71, and 1.77/2.24 V vs Mg^{2+}/Mg due to the multiple redox reactions upon Mg^{2+} (de)intercalation. In the following two scans, some changes can be observed, such as the broad reduction peak at 2.14 V gradually shifting to 2.18 V with a slight decrease in intensity; the reduction/oxidation peak at 1.77/2.24 V strongly decreases its intensity. In stark contrast, both V_2O_5 and CaVOnH exhibit CV profiles. For example, V_2O_5 displays two very broad reduction peaks (2.25 and 1.76 V) and one oxidation peak at 3.0 V for the first scan and a large irreversible capacity with notable changes in the shape and positions of both reduction and oxidation peaks in the following two scans.[14] Meanwhile, CaVOnH presents three broad reduction peaks (2.6, 2.2, and 1.8 V), three broad oxidation peaks (2.3, 2.73, and 3.14 V), and good electrochemical reversibility with slight changes in the shape and position of reduction and oxidation peaks in the following scans.[15] CV curves of

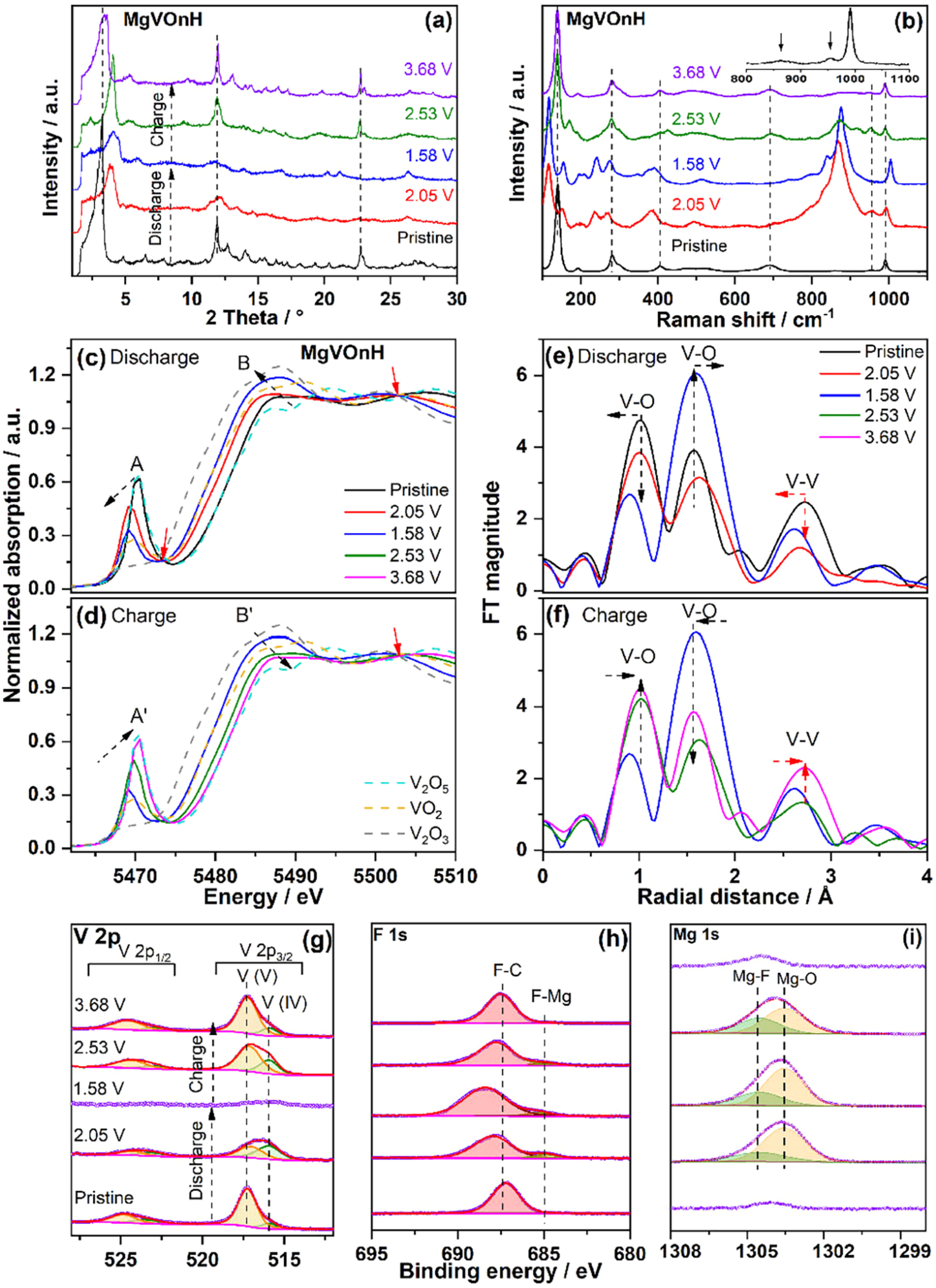

Figure 4. Ex situ XRD (a), Raman spectra ((b), inset enlarged Raman of pristine MgVOnH), X-ray absorption near-edge spectroscopy (XANES) (c, d) for the V K-edge, phase-uncorrected Fourier transforms (FT) (e, f) of V K-edge extended X-ray absorption fine structure (EXAFS) (k^3-weighted), and V 2p, F 1s, and Mg 1s X-ray photoelectron spectra (g, h, i) of MgVOnH at various discharge/charge states, respectively; the isosbestic points (c, d) are pointed out by solid red arrows.

MgVOnH at different scan rates are displayed in Figure 2b. Along with the increase in the scan rate, the overall CVs of MgVOnH maintain characteristic anodic/cathodic features despite progressive peak broadening and potential shifts. In general, peak current (i) and scan rate (ν) demonstrate a characteristic power-law dependence[14] of $i = a\nu^b$. By analyzing the linear fitting of lg(i) vs lg(ν), MgVOnH shows b values of 0.57/0.62 for the oxidation/reduction peaks, respectively (Figure 2c). Therefore, MgVOnH, V_2O_5, and CaVOnH demonstrate a diffusion-controlled process due to their similar b values, despite their different CV curves. Furthermore, the larger specific surface area of the material facilitates electrolyte penetration and enhances ion transport. High specific surface area and tailored mesoporosity in MgVOnH synergize with structural water to accelerate MgVOnH diffusion by reducing energy barriers and providing efficient ion pathways.

The electrochemical properties of MgVOnH were studied in the 0.8 m $Mg(TFSI)_2$−85% PEG−15% H_2O electrolyte under galvanostatic charge and discharge conditions, which were compared with those of V_2O_5 and CaVOnH, as summarized in Table S1. MgVOnH shows three clear plateaus (one short at 2.86 V, two long at 2.28 and 1.93 V) on the voltage−time profile and three clear plateaus (two long at 2.19 and 2.51 V and one short at 3.08 V) on the charge profiles (Figure 3a).

MgVOnH exhibits the first discharge/charge capacity of 268/276 mAh g^{-1} at 50 mA g^{-1}, leading to an initial Coulombic efficiency (CE) of ~103%, which can be attributed to minor Mg^{2+} extraction (~0.03 Mg^{2+}) from the original structure, accompanied by irreversible oxidation of the positive electrode. Afterward, it exhibits a second discharge capacity of 249 mAh g^{-1} and a capacity decrease to 201 mAh g^{-1} after 100 cycles, resulting in 81% capacity retention (against second discharge capacity, Figure 3b). Along with the increased current densities, the material demonstrates larger electrode polarization, as shown in Figure 3c. At high current densities (500 and 1000 mA g^{-1}), it only shows one clear discharge plateau at around 1.8 V. The rate test (Figure 3d) reveals that MgVOnH provides discharge capacities of 242, 178, 143, 104, and 56 mAh g^{-1} at 50, 100, 200, 500, and 1000 mA g^{-1}, respectively. This suggests that MgVOnH shows an unsatisfying rate performance due to the low kinetic properties at high current densities, which is highly dependent on the ionic conductivity of the electrolyte and the host structure.

Afterward, the electrochemical performances of MgVOnH are investigated in an optimized DMSO-containing electrolyte in the same working potential range, 0.8 m $Mg(TFSI)_2$−65% PEG−20% DMSO−15% H_2O, which offers a much-improved ionic conductivity and viscosity without sacrificing its ESW (~3.6 V), as illustrated in our recent work.[15] The rate capability test (Figure 3d) shows that MgVOnH delivers slightly lower capacities at low current densities (50, 100, and 200 mA g^{-1}) and much-improved capacities at high current densities (500 and 1000 mA g^{-1}) compared to what was obtained in 0.8 m $Mg(TFSI)_2$−85% PEG−15% H_2O. The observed behavior is a recognized phenomenon in electrolyte engineering and stems from a trade-off between enhanced ion transport kinetics and interfacial stability. The primary role of DMSO is to facilitate faster ion transport and desolvation kinetics at the cathode interface. This is the dominant factor under high-rate conditions, leading to the excellent rate performance observed. However, this same interface may be less stable during prolonged, slow cycling (at 50 mA g^{-1}), leading to slight parasitic reactions and a thicker interphase that reduces the low-rate capacity. Moreover, MgVOnH (Figure 3e) delivers an initial discharge capacity of 106 mAh g^{-1} at 1000 mA g^{-1} and discharge capacities of 85 and 69 mAh g^{-1} after 920 and 2000 cycles, yielding a capacity retention of 80 and 65%, respectively. Meanwhile, the charge−discharge curves are very similar to those obtained at high current densities of 500 and 1000 mA g^{-1} (Figure 3f,c). Impressively, MgVOnH achieves its maximum capacity for the first cycle, while V_2O_5 requires up to 400 cycles to reach its highest capacity of 101 mAh g^{-1} (Figure S2), and CaVOnH needs about 100 cycles[15] to gain its highest capacity of 93 mAh g^{-1}, demonstrating that better kinetic properties in the MgVOnH structure are probably due to the shielding effect of crystal water. This result indicates that the electrochemical performance is critically determined by the electrolyte's ionic conductivity, along with the interplanar spacing and the presence of structural crystal water.

3.3. Reaction Mechanism of MgVOnH in AMIBs

To gain a deep understanding of the reaction mechanism of MgVOnH in AMIBs, multiple techniques, including synchrotron-based absorption spectroscopy, were employed. First, ex situ XRD was carried out on MgVOnH samples at different discharge/charge states to examine the structure evolution during Mg^{2+} (de)intercalation (Figure 4a). After Mg^{2+} intercalation to 2.05 V, most reflections of MgVOnH move to lower angles, and the one at $2\theta = 3.2°$ shifts to a higher angle of 3.9° with strong intensity decrease and broadening, indicating the notable shrinking of interplanar layers and a 2-phase transition process during Mg^{2+} intercalation for the long plateau of 2.28 V. With further Mg^{2+} intercalation to 1.58 V, only a few very broad reflections at 4.3, 5.9, 8.2, 11.8, 13.9, 16.7, 20.3, 21.2, and 26.4° are observed, where the appearance of new reflections at 5.9, 13.9, 20.3, and 21.2° may suggest a second 2-phase transition process. Moreover, one small reflection ($2\theta = 2.4°$) appears and disappears during cycling. Upon charging to 2.53 V, all reflections are similar to the discharged state at 2.05 V, but with much stronger intensities, implying a reversible 2-phase transition. At 3.68 V, all main reflections return to their initial positions but with lower intensities, implying the 2-phase transition and high reversibility of MgVOnH.

To study the local structure evolution of MgVOnH during Mg^{2+} (de)intercalation, Raman scattering was conducted (Figure 4b). MgVOnH shares the typical Raman peaks of V_2O_5 as demonstrated in prior studies.[14,40] Additionally, two more Raman peaks at 862 and 954 cm^{-1} are observed for MgVOnH (inset of Figure 4b), probably due to the formation of the Mg−O bond, confirming local structure changes because of Mg^{2+} preintercalation. Following additional Mg^{2+} intercalation into MgVOnH (2.05 V), the peak of 140 cm^{-1} moves to 152 cm^{-1} with a significantly decreased intensity, and the other two peaks at 191 and 991 cm^{-1} shift to higher wavenumbers at 196 and 994 cm^{-1}, respectively, while two peaks at 281 and 406 cm^{-1} move toward lower wavenumbers at 270 and 385 cm^{-1}, respectively. Meanwhile, some new peaks appear at 115, 235, and 492 cm^{-1}, accompanied by the notable increase in the intensity of peaks at 869 and 954 cm^{-1}. As more Mg^{2+} ions are incorporated into MgVOnH (1.58 V), some peaks (235, 270, 385, 492, 869, and 994 cm^{-1}) shift to higher wavenumbers of 242, 274, 391, 511, 877, and 1005 cm^{-1}, respectively. The small peak at 954 cm^{-1} disappears, a new peak at 840 cm^{-1} appears, and the intensity of the peak at 115 cm^{-1} notably increases. These results demonstrate significant changes, such as Mg−O bonds in the local structure during Mg^{2+} intercalation. Upon charging to 2.53 and 3.68 V, it exhibits reversible peak variations and recovers to its initial state of MgVOnH, suggesting high reversibility of MgVOnH during cycling.

X-ray absorption spectroscopy (XAS) was conducted to probe the electronic and structural evolutions of V ions during electrochemical cycling. Figure 4c,d presents the normalized V K-edge spectra obtained throughout this process. The average oxidation state of V in pristine MgVOnH is determined as +4.87 by applying a linear-combination fitting (LCF) analysis (Figure S3), consistent with XPS analysis (Figure 4g). Additionally, it presents a pronounced pre-edge feature for the V K-edge, which is characteristic of vanadium in 5-fold oxygen coordination. This arises from dipole-transition-derived electronic excitations between 1s and bound p-hybridized d-states.[41,42] The similar XAS feature between MgVOnH and the xerogel material suggests a similar structure between MgVOnH and e-V_2O_5.[35] Upon discharging to 2.05 and 1.58 V, the V K-edge edge energy and pre-edge feature progressively move to lower energies, indicating the reduction of V ions to the predominant V^{4+} oxidation state (Figure 4c). The pre-edge intensity notably decreases, indicating an increase in the symmetry of V ions after Mg^{2+} intercalation.[41,42] Meanwhile, two broad peaks (5488 and 5491 eV, inset of Figure 4c indicated by black dashed arrows) of edge resonance (B) evolve to a single, intense broad peak centered at 5488 eV, which is attributed to electronic excitations involving core-level absorption.[42] Furthermore, distinct isosbestic points indicated by red solid arrows in Figure 4c,d imply a 2-phase reaction[43] during discharge and charge processes. At 1.58 V, the V K-edge spectrum almost overlaps with the standard reference VO_2, implying that the oxidation state of V is mainly V^{4+}. Upon charging to 2.53 and 3.68 V (Figure 4d), the main features of the V K-edge show reversible behaviors, suggesting that the oxidation of V ions occurs concurrently with Mg^{2+} deintercalation and reflecting a highly reversible local structural evolution. To further probe changes in the vanadium ion coordination environment, phase-uncorrected Fourier transforms (FT) of the k^3-weighted V K-edge extended X-ray absorption fine structure (EXAFS) spectra were analyzed. Two FT peaks corresponding to the V−O bonds in VO_6 octahedra at 1.02 and 1.57 Å and one FT peak assigned to the V−V shell at 2.73 Å are obtained for the pristine MgVOnH.[44−46] During discharging to 2.05 and 1.58 V, the peak at 1.03 Å shifts to lower radial distances with the decrease in intensity, and the peak at 1.64 Å shifts to higher radial distances with significantly increased amplitudes (Figure 4e, black dashed arrows), implying the increased symmetry in the local structure surrounding V. At the same time, the V−V feature moves to a lower value (red dashed arrows) with an amplitude decrease. These results identify that both V−O and V−V shell structures are impacted by the intercalated Mg^{2+} ions. During charging to 2.53 and 3.68 V, the spectrum presents reversible behavior and returns to its original position (Figure 4f), confirming the highly reversible local structural evolution of MgVOnH.

To further investigate the surface chemistry and elemental states of the electrodes before and after cycling, X-ray photoelectron spectroscopy (XPS) measurements were conducted (Figure 4g−i). In the pristine MgVOnH electrode, the V 2p spectrum was deconvoluted into two doublets, with V $2p_{3/2}$ peaks located at 517.2 and 515.9 eV,[39] corresponding to an average vanadium oxidation state of +4.89. Upon discharging to 2.05 V, the V ions are reduced to $V^{4.44+}$ with decreased V $2p_{3/2}$ peak intensity, and the V $2p_{3/2}$ peak completely disappears at 1.58 V, indicating the formation of a cathode electrolyte interphase (CEI) layer on the electrode surface. For pristine MgVOnH, the F 1s spectrum displays one peak at 687.3 eV associated with the C−F bond of the PVDF binder (Figure 4h). Upon discharge, F 1s spectra exhibit an additional peak at 684.9 eV (referring to the F−Mg bond), which is consistent with F^- in metal fluorides (such as MgF_2).[47] Meanwhile, Mg 1s spectra can be deconvoluted into two primary components: a main one with Mg 1s at 1304.5 and 1303.6 eV (referring to the Mg−F and Mg−O bonds, respectively).[47−49] The results reveal that MgF_2 is one of the main components of the CEI film because of the decomposition of the $TFSI^-$ anion. When charging to 2.53 and 3.68 V, the V $2p_{3/2}$ peak reoccurs with increased intensity, corresponding to vanadium oxidation states of +4.62 and +4.84, respectively. Note that the decrease/increase of the V $2p_{3/2}$ peak correlates with the increase/decrease of additional Mg 1s and F 1s peaks, suggesting the reversible formation/decomposition of the CEI film accompanied by the reduction/oxidation of V ions during cycling.

In summary, bilayered MgVOnH undergoes significant structure changes in long and local ranges as well as electron compensation during Mg^{2+} (de)intercalation, such as a two-phase transition reaction with notable shrinking/expansion of interplanar layers, notably pre-edge peak, and symmetry decrease/increase, and CEI formation/decomposition.

4. CONCLUSIONS

Oxygen-rich bilayered MgVOnH was prepared via a hydrothermal method. MgVOnH holds multiple redox reaction peaks at 3.18/3.31, 2.86/3.14, 2.14/2.71, and 1.77/2.24 V vs Mg^{2+}/Mg due to the multiple redox reactions with the reduction of V to V^{4+} upon Mg^{2+} (de)intercalation. In 0.8 m $Mg(TFSI)_2$−85% PEG−15% H_2O, the MgVOnH positive electrode exhibits promising electrochemical performance, achieving an initial high discharge capacity of 268 mAh g^{-1} and a second discharge capacity of 249 mAh g^{-1} at 50 mA g^{-1}. After 100 cycles, it retains a discharge capacity of 201 mAh g^{-1}, corresponding to 81% retention relative to the second cycle. Furthermore, MgVOnH exhibits much better rate capability and high capacity at high current (500 and 1000 mA g^{-1}) in the DMSO-containing electrolyte. Particularly, MgVOnH shows a maximum specific capacity of 106 mAh g^{-1} for the first discharge at 1000 mA g^{-1} and yields a capacity retention of 80% after 920 cycles (85 mAh g^{-1}) and 65% after 2000 cycles (69 mAh g^{-1}) because of the crystal water and preintercalated Mg^{2+} with large interplanar spacing. The synergistic effects of the electrolyte's ionic conductivity, interplanar spacing adjustments, and structural crystal water significantly enhance electrochemical performance. In addition, the reaction mechanism and Mg^{2+} (de)intercalation reversibility of MgVOnH are carefully studied via ex situ techniques. These studies clearly elucidate the structural evolution, changes in the vanadium oxidation state, and local electronic environment. At the same time, the reversible formation and dissolution of CEI are observed, with MgF_2 identified as the primary component resulting from $TFSI^-$ anion decomposition. This work helps us to understand more about the mechanisms, and this can guide us in achieving a better design for advanced high-performance positive electrodes in multivalent aqueous batteries.

■ ASSOCIATED CONTENT

Supporting Information

The Supporting Information is available free of charge at https://pubs.acs.org/doi/10.1021/acsami.5c08636.

> SEM image and EDS mapping, cycling performance of V_2O_5 and MgVOnH, a linear-combination fitting (LCF) of the V K-edge XANES spectrum of pristine MgVOnH (Figures S1−S3), and comparison of the discharge capacities of three materials in two distinct electrolytes (Table S1) (PDF)

■ AUTHOR INFORMATION

Corresponding Author

Qiang Fu − *Institute for Applied Materials (IAM), Karlsruhe Institute of Technology (KIT), D-76344 Eggenstein-Leopoldshafen, Germany;* orcid.org/0000-0002-2507-5477; Phone: 49-721-608-41445; Email: qiang.fu@kit.edu; Fax: 49-721-608-28521

Authors

Xianlin Luo − *Institute for Applied Materials (IAM), Karlsruhe Institute of Technology (KIT), D-76344 Eggenstein-Leopoldshafen, Germany*

Liwen Yang − *Institute for Applied Materials (IAM), Karlsruhe Institute of Technology (KIT), D-76344 Eggenstein-Leopoldshafen, Germany*

Angelina Sarapulova − *Institute for Applied Materials (IAM), Karlsruhe Institute of Technology (KIT), D-76344 Eggenstein-Leopoldshafen, Germany; Department of Electrical Energy Storage, Fraunhofer Institute for Solar Energy Systems, 79110 Freiburg, Germany; FMF-Freiburg Materials Research Center, University of Freiburg, 79104 Freiburg, Germany*

Michael Knapp − *Institute for Applied Materials (IAM), Karlsruhe Institute of Technology (KIT), D-76344 Eggenstein-Leopoldshafen, Germany;* orcid.org/0000-0003-0091-8463

Helmut Ehrenberg − *Institute for Applied Materials (IAM), Karlsruhe Institute of Technology (KIT), D-76344 Eggenstein-Leopoldshafen, Germany;* orcid.org/0000-0002-5134-7130

Sonia Dsoke − *Institute for Applied Materials (IAM), Karlsruhe Institute of Technology (KIT), D-76344 Eggenstein-Leopoldshafen, Germany; Department of Electrical Energy Storage, Fraunhofer Institute for Solar Energy Systems, 79110 Freiburg, Germany; FMF-Freiburg Materials Research Center, University of Freiburg, 79104 Freiburg, Germany; Institute for Sustainable Systems Engineering (INATECH), University of Freiburg, 79110 Freiburg, Germany*

Complete contact information is available at: https://pubs.acs.org/10.1021/acsami.5c08636

Notes

The authors declare no competing financial interest.

ACKNOWLEDGMENTS

This work contributes to the research performed at CELEST (Center for Electrochemical Energy Storage Ulm-Karlsruhe) and was partially funded by the German Research Foundation (DFG) under Project ID 390874152 (POLiS Cluster of Excellence). We acknowledge the synchrotron radiation source Petra-III (DESY) in Hamburg, Germany, for the provision of beamtime at the P65 beamline. We would like to thank Dr. Edmund Welter from Experiments Division at DESY, Hamburg. We thank Bettina Hunzinger and Dennis Triller for their support in SEM and EDS measurements. We greatly appreciate Liuda Mereacre for her support in TGA and Raman measurements. Dr. Thomas Bergfeldt (IAM-AWP) is gratefully acknowledged for ICP-OES measurements.

REFERENCES

(1) Mao, M.; Gao, T.; Hou, S.; Wang, C. A Critical Review of Cathodes for Rechargeable Mg Batteries. *Chem. Soc. Rev.* **2018**, *47* (23), 8804−8841.

(2) Wang, F.; Fan, X.; Gao, T.; Sun, W.; Ma, Z.; Yang, C.; Han, F.; Xu, K.; Wang, C. High-Voltage Aqueous Magnesium Ion Batteries. *ACS Cent. Sci.* **2017**, *3* (10), 1121−1128.

(3) Wang, J.; Yu, R.; Wang, J.; Long, J.; Qiao, F.; Zhang, L.; He, G.; An, Q.; Mai, L. Bi Nanoparticles Encapsulated in Nitrogen-Doped Carbon as a Long-Life Anode Material for Magnesium Batteries. *J. Magnesium Alloys* **2023**, *11* (11), 4181−4188.

(4) Huang, M.; Wang, X.; Wang, J.; Meng, J.; Liu, X.; He, Q.; Geng, L.; An, Q.; Yang, J.; Mai, L. Proton/Mg^{2+} Co-Insertion Chemistry in Aqueous Mg-Ion Batteries: From the Interface to the Inner. *Angew. Chem., Int. Ed.* **2023**, *62* (37), No. e202308961.

(5) Zhang, Z.; Song, M.; Si, C.; Cui, W.; Wang, Y. Amorphous Germanium-Crystalline Bismuth Films as a Promising Anode for Magnesium-Ion Batteries. *eScience* **2023**, *3* (1), No. 100070.

(6) Kim, H.; Hong, J.; Park, K.-Y.; Kim, H.; Kim, S.-W.; Kang, K. Aqueous Rechargeable Li and Na Ion Batteries. *Chem. Rev.* **2014**, *114* (23), 11788−11827.

(7) Hu, B.; Li, D.; Li, M.; Jiang, J.; Zhao, Y.; Du, T.; Zhou, Z.; Pu, H.; Ma, G.; Li, Z. Dual Active Sites along with Hydrophobic Structure Modulation of Vanadium Hexacyanoferrate for Aqueous Zn-Ion Batteries. *Inorg. Chem.* **2025**, *64* (12), 6042−6052.

(8) Hu, B.; Li, D.; Li, M.; Jiang, J.; Zou, Y.; Deng, Y.; Zhou, Z.; Pu, H.; Ma, G.; Li, Z. Conductive Network Enhanced Self-Assembled Diphasic Prussian Blue Analogs for Aqueous Zinc-Ion Batteries. *J. Mater. Chem. C* **2025**, *13* (13), 6736−6744.

(9) Song, M.; Tan, H.; Chao, D.; Fan, H. J. Recent Advances in Zn-Ion Batteries. *Adv. Funct. Mater.* **2018**, *28* (41), No. 1802564.

(10) Xu, C.; Li, B.; Du, H.; Kang, F. Energetic Zinc Ion Chemistry: the Rechargeable Zinc Ion Battery. *Angew. Chem., Int. Ed.* **2012**, *51* (4), 933−935.

(11) Chen, L.; Bao, J. L.; Dong, X.; Truhlar, D. G.; Wang, Y.; Wang, C.; Xia, Y. Aqueous Mg-Ion Battery Based on Polyimide Anode and Prussian Blue Cathode. *ACS Energy Lett.* **2017**, *2* (5), 1115−1121.

(12) Zhu, Y.; Yin, J.; Emwas, A.-H.; Mohammed, O. F.; Alshareef, H. N. An Aqueous Mg^{2+}-Based Dual-Ion Battery with High Power Density. *Adv. Funct. Mater.* **2021**, *31* (50), No. 2107523.

(13) Zhu, Y.; Guo, X.; Lei, Y.; Wang, W.; Emwas, A.-H.; Yuan, Y.; He, Y.; Alshareef, H. N. Hydrated Eutectic Electrolytes for High-Performance Mg-Ion Batteries. *Energy Environ. Sci.* **2022**, *15* (3), 1282−1292.

(14) Fu, Q.; Wu, X.; Luo, X.; Indris, S.; Sarapulova, A.; Bauer, M.; Wang, Z.; Knapp, M.; Ehrenberg, H.; Wei, Y.; Dsoke, S. High-Voltage Aqueous Mg-Ion Batteries Enabled by Solvation Structure Reorganization. *Adv. Funct. Mater.* **2022**, *32* (16), No. 2110674.

(15) Fu, Q.; Wu, X.; Luo, X.; Ding, Z.; Indris, S.; Sarapulova, A.; Meng, Z.; Desmau, M.; Wang, Z.; Hua, W.; Kübel, C.; Schwarz, B.; Knapp, M.; Ehrenberg, H.; Wei, Y.; Dsoke, S. Ca^{2+} Pre-Intercalated Bilayered Vanadium Oxide for High-Performance Aqueous Mg-Ion Batteries. *Energy Storage Mater.* **2024**, *66*, No. 103212.

(16) Liu, Z.; Li, X.; He, J.; Wang, Q.; Zhu, D.; Yan, Y.; Chen, Y. Is Proton A Charge Carrier for δ-MnO_2 Cathode in Aqueous Rechargeable Magnesium-Ion Batteries? *J. Energy Chem.* **2022**, *68*, 572−579.

(17) Zhang, H.; Cao, D.; Bai, X. High Rate Performance of Aqueous Magnesium-Ion Batteries Based on the δ-MnO_2@Carbon Molecular Sieves Composite as the Cathode and Nanowire VO_2 as the Anode. *J. Power Sources* **2019**, *444*, No. 227299.

(18) Tekin, B.; Demir-Cakan, R. Understanding the Role of Water-Based Electrolytes on Magnesium-Ion Insertion/Extraction into Lambda-MnO_2 Lattice Structure. *Solid State Ionics* **2019**, *335*, 67−73.

(19) Pan, Z.; Qin, T.; Zhang, W.; Chu, X.; Dong, T.; Yue, N.; Wang, Z.; Zheng, W. Non-Layer-Transformed Mn_3O_4 Cathode Unlocks Optimal Aqueous Magnesium-Ion Storage via Synergizing Amorphous Ion Channels and Grain Refinement. *J. Energy Chem.* **2022**, *68*, 42−48.

(20) Liu, G.; Chi, Q.; Zhang, Y.; Chen, Q.; Zhang, C.; Zhu, K.; Cao, D. Superior High Rate Capability of $MgMn_2O_4$/rGO Nanocomposites as Cathode Materials for Aqueous Rechargeable Magnesium Ion Batteries. *Chem. Commun.* **2018**, *54* (68), 9474−9477.

(21) Wen, B.; Yang, C.; Wu, J.; Liu, J.; Wang, W.; Yang, J.; Chi, X.; Liu, Y. Water-Induced 3D $MgMn_2O_4$ Assisted by Unique Nanofluidic Effect for Energy-Dense and Durable Aqueous Magnesium-Ion Batteries. *Chem. Eng. J.* **2022**, *435*, No. 134997.

(22) Zhang, H.; Ye, K.; Huang, X.; Wang, X.; Cheng, K.; Xiao, X.; Wang, G.; Cao, D. Preparation of $Mg_{1.1}Mn_6O_{12}\cdot4.5H_2O$ with

Nanobelt Structure and Its Application in Aqueous Magnesium-Ion Battery. *J. Power Sources* **2017**, *338*, 136−144.

(23) Zhang, Y.; Liu, G.; Zhang, C.; Chi, Q.; Zhang, T.; Feng, Y.; Zhu, K.; Zhang, Y.; Chen, Q.; Cao, D. Low-Cost $MgFe_xMn_{2-x}O_4$ Cathode Materials for High-Performance Aqueous Rechargeable Magnesium-Ion Batteries. *Chem. Eng. J.* **2020**, *392*, No. 123652.

(24) Andrews, J. L.; Mukherjee, A.; Yoo, H. D.; Parija, A.; Marley, P. M.; Fakra, S.; Prendergast, D.; Cabana, J.; Klie, R. F.; Banerjee, S. Reversible Mg-Ion Insertion in a Metastable One-Dimensional Polymorph of V_2O_5. *Chem* **2018**, *4* (3), 564−585.

(25) Yoo, H. D.; Jokisaari, J. R.; Yu, Y.-S.; Kwon, B. J.; Hu, L.; Kim, S.; Han, S.-D.; Lopez, M.; Lapidus, S. H.; Nolis, G. M.; Ingram, B. J.; Bolotin, I.; Ahmed, S.; Klie, R. F.; Vaughey, J. T.; Fister, T. T.; Cabana, J. Intercalation of Magnesium into a Layered Vanadium Oxide with High Capacity. *ACS Energy Lett.* **2019**, *4* (7), 1528−1534.

(26) Deng, X.; Xu, Y.; An, Q.; Xiong, F.; Tan, S.; Wu, L.; Mai, L. Manganese Ion Pre-Intercalated Hydrated Vanadium Oxide as a High-Performance Cathode for Magnesium Ion Batteries. *J. Mater. Chem. A* **2019**, *7* (17), 10644−10650.

(27) Xu, Y.; Deng, X.; Li, Q.; Zhang, G.; Xiong, F.; Tan, S.; Wei, Q.; Lu, J.; Li, J.; An, Q.; Mai, L. Vanadium Oxide Pillared by Interlayer Mg^{2+} Ions and Water as Ultralong-Life Cathodes for Magnesium-Ion Batteries. *Chem* **2019**, *5* (5), 1194−1209.

(28) Gomes, S.; Nedelec, J.-M.; Jallot, E.; Sheptyakov, D.; Renaudin, G. Unexpected Mechanism of Zn^{2+} Insertion in Calcium Phosphate Bioceramics. *Chem. Mater.* **2011**, *23* (12), 3072−3085.

(29) Parry, K. L.; Shard, A. G.; Short, R. D.; White, R. G.; Whittle, J. D.; Wright, A. ARXPS Characterisation of Plasma Polymerised Surface Chemical Gradients. *Surf. Interface Anal.* **2006**, *38* (11), 1497−1504.

(30) Scofield, J. H. Hartree-Slater Subshell Photoionization Cross-Sections at 1254 and 1487 eV. *J. Electron Spectrosc. Relat. Phenom.* **1976**, *8* (2), 129−137.

(31) Tanuma, S.; Powell, C. J.; Penn, D. R. Calculations of Electron Inelastic Mean Free Paths. IX. Data for 41 Elemental Solids over the 50 eV to 30 keV Range. *Surf. Interface Anal.* **2011**, *43* (3), 689−713.

(32) Ravel, B.; Newville, M. ATHENA, ARTEMIS, HEPHAESTUS: Data Analysis for X-ray Absorption Spectroscopy using IFEFFIT. *J. Synchrotron Radiat.* **2005**, *12* (4), 537−541.

(33) Oka, Y.; Yao, T.; Yamamoto, N. Crystal Structures of Hydrated Vanadium Oxides withδ-Type V_2O_5 Layers:δ-$M_{0.25}V_2O_5{\cdot}H_2O$,M = Ca, Ni. *J. Solid State Chem.* **1997**, *132* (2), 323−329.

(34) Oka, Y.; Yao, T.; Yamamoto, N. Crystal Structures and Lattice Distortions of σ-Type Layered Vanadium Bronzes:σ-$M_{0.25}V_2O_5{\cdot}H_2O$ (M = Mg, Co, Ni). *J. Solid State Chem.* **1999**, *144* (1), 181−187.

(35) Potiron, E.; Le Gal La Salle, A.; Verbaere, A.; Piffard, Y.; Guyomard, D. Electrochemically Synthesized Vanadium Oxides as Lithium Insertion Hosts. *Electrochim. Acta* **1999**, *45* (1), 197−214.

(36) Potiron, E.; Le Gal La Salle, A.; Verbaere, A.; Piffard, Y.; Guyomard, D.; Tournoux, M. Electrochemical Synthesis, Characterization and Lithium Intercalation Properties of e-$M_xV_2O_{5+y}$.nH_2O (M = NiII, CuII or MnIV). *J. Phys. Chem. Solids* **2001**, *62* (8), 1447−1455.

(37) Esparcia, E. A.; Chae, M. S.; Ocon, J. D.; Hong, S.-T. Ammonium Vanadium Bronze ($NH_4V_4O_{10}$) as a High-Capacity Cathode Material for Nonaqueous Magnesium-Ion Batteries. *Chem. Mater.* **2018**, *30* (11), 3690−3696.

(38) Kundu, D.; Adams, B. D.; Duffort, V.; Vajargah, S. H.; Nazar, L. F. A High-Capacity and Long-Life Aqueous Rechargeable Zinc Battery Using a Metal Oxide Intercalation Cathode. *Nat. Energy* **2016**, *1* (10), No. 16119.

(39) Silversmit, G.; Depla, D.; Poelman, H.; Marin, G. B.; De Gryse, R. Determination of the V2p XPS Binding Energies for Different Vanadium Oxidation States (V^{5+} to V^{0+}). *J. Electron Spectrosc. Relat. Phenom.* **2004**, *135* (2−3), 167−175.

(40) Baddour-Hadjean, R.; Pereira-Ramos, J. P.; Navone, C.; Smirnov, M. Raman Microspectrometry Study of Electrochemical Lithium Intercalation into Sputtered Crystalline V_2O_5 Thin Films. *Chem. Mater.* **2008**, *20* (5), 1916−1923.

(41) Tanaka, T.; Yamashita, H.; Tsuchitani, R.; Funabiki, T.; Yoshida, S. X-ray Absorption (EXAFS/XANES) Study of Supported Vanadium Oxide Catalysts. Structure of Surface Vanadium Oxide Species on Silica and [gamma]-Alumina at a Low Level of Vanadium Loading. *J. Chem. Soc., Faraday Trans. 1* **1988**, *84* (9), 2987−2999.

(42) Wong, J.; Lytle, F. W.; Messmer, R. P.; Maylotte, D. H. K-Edge Absorption Spectra of Selected Vanadium Compounds. *Phys. Rev. B* **1984**, *30* (10), 5596−5610.

(43) Liu, X.; Wang, D.; Liu, G.; Srinivasan, V.; Liu, Z.; Hussain, Z.; Yang, W. Distinct Charge Dynamics in Battery Electrodes Revealed by In Situ and Operando Soft X-ray Spectroscopy. *Nat. Commun.* **2013**, *4*, No. 2568.

(44) Stizza, S.; Mancini, G.; Benfatto, M.; Natoli, C. R.; Garcia, J.; Bianconi, A. Structure of Oriented V_2O_5 Gel Studied by Polarized X-Ray-Absorption Spectroscopy at the Vanadium K Edge. *Phys. Rev. B* **1989**, *40* (18), 12229−12236.

(45) Mansour, A. N.; Smith, P. H.; Balasubramanian, M.; McBreen, J. *In Situ* X-Ray Absorption Study of Cycled Ambigel $V_2O_5{\cdot}nH_2O(n{\approx}0.5)$ Composite Cathodes. *J. Electrochem. Soc.* **2005**, *152* (7), A1312.

(46) Giorgetti, M.; Passerini, S.; Smyrl, W. H.; et al. *In Situ* X-Ray Absorption Spectroscopy Characterization of V_2O_5 Xerogel Cathodes upon Lithium Intercalation. *J. Electrochem. Soc.* **1999**, *146* (7), 2387.

(47) Liu, X.; Wen, J.; Zhao, X.; Shang, B.; Lei, J.; Li, L.; Pan, F. Innovative Fluorinated Boron-Based Electrolyte Harmonizes Interface Chemistry-Electrochemistry of Mg Anode for Accessible Rechargeable Mg Battery. *Chem. Eng. J.* **2025**, *518*, No. 164545.

(48) Zhang, J.; Guan, X.; Lv, R.; Wang, D.; Liu, P.; Luo, J. Rechargeable Mg Metal Batteries Enabled by a Protection Layer Formed in Vivo. *Energy Storage Mater.* **2020**, *26*, 408−413.

(49) Hou, S.; Ji, X.; Gaskell, K.; Wang, P.-f.; Wang, L.; Xu, J.; Sun, R.; Borodin, O.; Wang, C. Solvation Sheath Reorganization Enables Divalent Metal Batteries with Fast Interfacial Charge Transfer Kinetics. *Science* **2021**, *374* (6564), 172−178.